Acta Pharmaceutica Sinica B 2023;13(11):4578–4590

Chinese Pharmaceutical Association
Institute of Materia Medica, Chinese Academy of Medical Sciences

Acta Pharmaceutica Sinica B

www.elsevier.com/locate/apsb
www.sciencedirect.com

ORIGINAL ARTICLE

Novel NIR-II fluorescent probes for biliary atresia imaging

Xiaodong Zeng[a,e,g,†], Yuqin Liao[a,b,c,†], Xue Qiao[a,d], Ke Liang[a,e], Qiusi Luo[a,b,c], Mingbo Deng[a,b,c], Yishen Liu[a,b,c], Weijing Zhang[b,c,f], Xuechuan Hong[a,d,e], Yuling Xiao[a,b,c,*]

[a]*State Key Laboratory of Virology, Department of Cardiology, Zhongnan Hospital of Wuhan University, School of Pharmaceutical Sciences, Wuhan University, Wuhan 430071, China*
[b]*State Key Laboratory of Drug Research & Center of Pharmaceutics, Shanghai Institute of Materia Medica, Chinese Academy of Sciences, Shanghai 201203, China*
[c]*Shandong Laboratory of Yantai Drug Discovery, Bohai Rim Advanced Research Institute for Drug Discovery, Yantai 264117, China*
[d]*Key Laboratory of Biodiversity and Environment on the Qinghai-Tibetan Plateau, Ministry of Education, School of Ecology and Environment, Tibet University, Lhasa 850000, China*
[e]*Shenzhen Institute of Wuhan University, Shenzhen 518057, China*
[f]*School of Pharmacy, Yantai University, Yantai 264005, China*
[g]*School of Biomedical Engineering, Shanghai Jiao Tong University, Shanghai 200240, China*

Received 5 March 2023; received in revised form 26 May 2023; accepted 27 June 2023

KEY WORDS

Biliary atresia;
Fluorescence imaging;
Second near-infrared window;
Early diagnosis;
Hepatobiliary excretion

Abstract Biliary atresia is a rare infant disease that predisposes patients to liver transplantation and death if not treated in time. However, early diagnosis is challenging because the clinical manifestations and laboratory tests of biliary atresia overlap with other cholestatic diseases. Therefore, it is very important to develop a simple, safe and reliable method for the early diagnosis of biliary atresia. Herein, a novel NIR-II fluorescence probe, HZL2, with high quantum yield, excellent biocompatibility, low cytotoxicity and rapid excretion through the liver and gallbladder was developed based on the oil/water partition coefficient and permeability. A simple fecal sample after injection of HZL2 can be used to efficiently identify the success of the mouse model of biliary atresia for the first time, allowing for an early diagnosis of the disease. This study not only developed a simple and safe method for the early diagnosis of biliary atresia with great potential in clinical translation but also provides a research tool for the development of pathogenesis and therapeutic medicines for biliary atresia.

*Corresponding author.
E-mail address: xiaoyl@whu.edu.cn (Yuling Xiao).
[†]These authors contributed equally to this work.
Peer review under responsibility of Chinese Pharmaceutical Association and Institute of Materia Medica, Chinese Academy of Medical Sciences.

https://doi.org/10.1016/j.apsb.2023.07.005

1. Introduction

Biliary atresia is a rare, severe inflammatory and obliterative cholangiopathy that affects millions of infants[1]. The inflammatory process of biliary atresia leads to bile duct fibrosis, cholestasis, progressive liver fibrosis and liver cirrhosis, which further causes liver failure and mortality in children under the age of two if left untreated[2]. Optimal outcomes for neonates are contingent upon early identification, referral and timely Kasai portoenterostomy. The likelihood of success of Kasai surgery decreases with delay[3,4]. Therefore, early diagnosis and timely surgical treatment of biliary atresia are essential. Although the pathophysiology of biliary atresia remains unknown, several mechanisms have been proposed, including genetic susceptibility and immune dysregulation, as well as congenital malformations, congenital cytomegalovirus infection and reovirus infection[5−7]. The causes of persistent jaundice in infants are different, making it difficult to accurately identify biliary atresia by routine blood examination[8]. In the clinic, ^{99}mTc-mebrofenin hepatobiliary scintigraphy was initially performed to rule out biliary atresia before definitive diagnosis *via* an invasive intraoperative cholangiogram[9]. However, exposure to ionizing radiation has been demonstrated to increase the risk of childhood leukemia. Misinterpretations of hepatobiliary scintigraphy led to delayed diagnosis and surgical palliation with Kasai portoenterostomy for biliary atresia[10,11]. There is an unmet clinical need for a safe and reliable approach for the early detection of biliary atresia.

Recently, fluorescence imaging in the second near-infrared window (NIR-II, 1000−1700 nm) has shown great promise in biomedical applications for disease diagnosis and image-guided therapy with deeper penetration depth and higher resolution compared to visible and NIR-I (700−900 nm) windows due to less photon absorption and scattering and negligible autofluorescence of biological tissues in the NIR-II window[12−26]. The first trial in humans of NIR-II fluorescence navigation in liver cancer surgery demonstrates that NIR-II fluorescence imaging has great potential for clinical application[27]. At present, numerous NIR-II fluorescence imaging contrast agents have been reported for use in a variety of biomedical applications, including small-molecule dyes[28,29] and conjugated polymers[30], inorganic nanomaterials such as gold nanomaterials[31,32], single-walled carbon nanotubes (SWCNTs)[33], quantum dots (QDs)[34], and rare earth-doped nanoparticles (RENPs)[35]. To the best of our knowledge, no NIR-II fluorophores excreted by the hepatobiliary system have been reported for NIR-II imaging and early diagnosis of biliary atresia.

Herein, for the first time, we demonstrate the rational design for the construction of a series of NIR-II fluorophores excreted by the hepatobiliary pathway based on the oil/water partition coefficient and permeability (Scheme 1). The semiquantitative NIR-II fluorescent analysis of the liver to leg tissue (L/L) or the bladder to leg tissue (B/L) and 24-h excreted urine or feces with CH1055a-c and H3a-c demonstrated that an NIR-II dye H3a with a fluorene moiety, mainly excreted by the liver, corresponded to the high log*P* value (−0.41). The benzyl group was then integrated into the sp^3 carbon of the fluorene group of H3 to identify a novel NIR-II probe, HZL, with enhanced lipid solubility and improved pharmacokinetic features (Scheme 1A). The PEGylated NIR-II fluorescent probe HZL2 with the fastest hepatobiliary excretion rate self-assembled into stable micelles in aqueous solution (critical aggregation concentration, CAC, 0.140 mg/mL). HZL2 exhibited suitable log*P*, XLOGP2, XLOGP3 and miLog*P* values and a superior hepatobiliary excretion capacity (∼80%). Furthermore, high-resolution NIR-II imaging of the murine bile duct stricture (BDS) and bile duct ligation (BDL) models of biliary atresia using HZL2 was successfully achieved for the first time (Scheme 1B). This study illustrates that HZL2 is promising for clinical translation of the noninvasive early detection of biliary atresia with a simple fecal sample (Scheme 1).

2. Materials and methods

2.1. Materials and general procedure

$NH_2(CH_2CH_2O)_nMe$ (approximately 0.35, 0.57, 0.93 and 1.98 kDa) was purchased from Ponsure Biotechnology Co., Ltd. The synthetic reagents were purchased from commercial suppliers (such as Aldrich, Energy Chemical, and Sinopharm Group Co., Ltd.) and used without further purification. The tetracarboxylic acid compound derived from H3, CH1055, and 4,7-bis(7-bromo-2,3-dihydrothieno[3,4-*b*][1,4]dioxin-5-yl)-5,6-dinitrobenzo[*c*][1,2,5]thiadiazole were synthesized according to our previous report[36,37]. ^{1}H NMR and ^{13}C NMR spectra were recorded in $CDCl_3$ at room temperature using a Bruker AV400 magnetic resonance spectrometer. MALDI-TOF-MS characteristics were determined on an AB SCIEX 5800 MALDI TOF mass spectrometer. UV−Vis NIR spectra were tested with a SHIMADZU UV-2600 or PerkinElmer Lambda 25 spectrophotometer. NIR fluorescence spectroscopy was performed on an Applied NanoFluorescence spectrometer at ambient temperature with an excitation laser source of 808 nm. The size and shape of HZL1−3 aggregates were observed by a Hitachi HT7700 transmission electron microscopy. The dynamic light scattering (DLS) and the zeta potential of the aggregates were measured using a Malvern Zetasizer Nano ZS90. The NIR-II *in vivo* imaging system was purchased from Suzhou NIR-Optics Technologies Co., Ltd.

2.2. Preparation and identification of NIR-II fluorescent probes

All NIR-II fluorescent probes were prepared in a concise pathway. The detailed synthetic procedure and the identification information can be found in the Supporting Information.

2.3. Determination of the oil-water partition coefficient

UV−Vis spectroscopy was used to determine the oil-water partition coefficients of CH1055a-c, H3a-c, and HZL1−3 in the *n*-octanol/water system through the shaking flask method. Briefly,

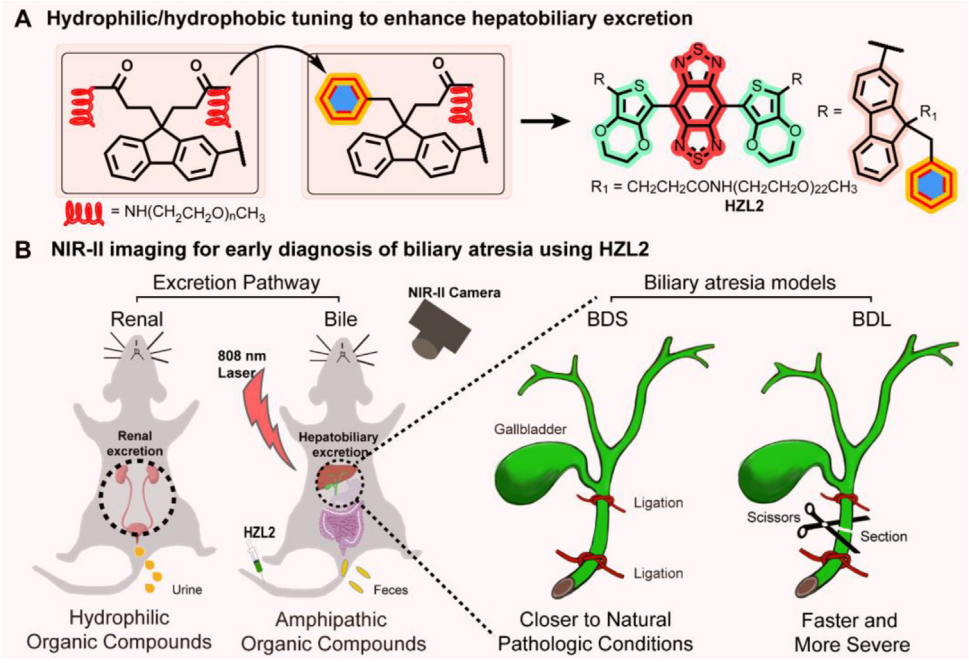

Scheme 1 (A) Schematic illustration of the discovery procedure of hepatobiliary excretion NIR-II probe HZL2. (B) Molecular properties of hepatobiliary and renal excretion, and schematic illustration of NIR-II imaging for biliary atresia models.

the saturated aqueous solution containing all the previously mentioned compounds and *n*-octanol was mixed well in a capped conical flask for 24 h. After equilibrium, the content of all of the compounds in the aqueous and *n*-octanol phase solutions was measured through the standard curves for the oil-water partition coefficient calculation.

2.4. *Fluorescence quantum yield measurement*

The fluorescence quantum yield measurement was reported in our previous work[38], and IR-26 was used as the reference with 0.5% quantum yield in DCE. The quantum yield was calculated as Eq. (1):

$$QY_{sample} = QY_{IR26} \times \frac{Slope_{sample}}{Slope_{IR26}} \times \frac{n^2_{sample}}{n^2_{IR26}} \quad (1)$$

where QY_{sample} is the QY of the fluorophore dissolved in solvent, QY_{IR26} is the QY of IR-26 in DCE, and n_{sample} and n_{IR26} are the refractive indices of the solvent (DCM or water) and DCE, respectively.

2.5. *Critical aggregation concentration (CAC) measurement*

Various concentrations of HZL1−3 (0.01−1.5 mg/mL) in deionized water were prepared. The transmittance of the solutions was then measured by UV−Vis spectroscopy, and a correlation was established between the solution concentration and transmittance at their maximum absorption wavelength to calculate the CAC.

2.6. *Transmission electron microscopy (TEM), DLS and zeta potential*

TEM (Hitachi HT7700) was used to examine the morphology of HZL1−3. To create TEM specimens, an aqueous solution of HZL1−3 was added dropwise onto carbon-coated grids (Cu, 400 mesh) and dried naturally. HZL1−3 aqueous solutions (∼0.5 mg/mL) were used for DLS and zeta potential measurements with a Malvern Zetasizer Nano ZS90 at room temperature.

2.7. *Cell culture and animals*

Human hepatic cells (L02) were obtained from the China Center for Type Culture Collection (CCTCC). L02 cells were cultured in RPMI 1640 medium with 10% (*v*/*v*) fetal bovine serum (FBS), 100 IU/mL penicillin, and 100 μg/mL streptomycin in a humidified atmosphere with 5% CO_2 at 37 °C. All female Kunming (KM) mice were purchased from Hunan SJA Laboratory Animal Co., Ltd. and were used under the guidance of the Institutional Animal Care and Use Committee (IACUC) of Wuhan University.

2.8. *Cytotoxicity evaluation*

The cytotoxicity of HZL1−3 was determined by using the CCK-8 assay. The L02 cells were seeded into 96-well plates at a density of 5×10^3 cells per well and incubated for 24 h. Subsequently, the medium was replaced by 100 μL of fresh medium with HZL1, HZL2, or HZL3 at different concentrations (0, 10, 20, 30, 40, and 50 μmol/L). After 24 h of incubation, the cell viability was

evaluated by the CCK-8 assay according to the protocol, and the optical density was measured at 450 nm by a microplate reader. The cytotoxicity experiments were repeated three times.

2.9. Calcein-AM/PI staining

The L02 cells were treated with different concentrations (10, 30, 50 μmol/L) of HZL1−3 or doxorubicin for 24 h. The culture was removed, and the cells were gently rinsed with PBS (200 μL) and then stained with 200 μL of calcein-AM/PI solution. The L02 cells were cultured in a cell incubator at 37 °C for 30 min before live/dead cell imaging using an inverted fluorescence microscope (Olympus, USA).

2.10. Determination of blood half-life

Healthy female KM mice were randomly separated into four groups and given an intravenous (i.v.) injection of H3a or HZL1−3 (n = 3, 15 mg/kg, 200 μL) to evaluate their pharmacokinetics. Blood samples with anticoagulants were obtained at predefined intervals (5, 10, 15, 20, 30, 60, 120, 240, 360, 480, 600, 720, and 1440 min). The samples were imaged using the NIR-II fluorescence imaging system (808 nm laser, 1000 nm LP filter, 90 mW/cm^2). The fluorescence intensity of the blood samples was measured using ImageJ software for the blood half-life calculation. The time-dependent relative fluorescence intensity in blood was fitted with a first-order exponential decay.

2.11. Hepatobiliary and urinary excretion studies

Healthy female KM mice were randomly separated into nine groups and anesthetized with pentobarbital sodium solution (50 mg/kg) before imaging with long-pass filters (1000 nm) under 808 nm laser irradiation (90 mW/cm^2) using an NIR-II *in vivo* imaging system. CH1055a-c, H3a-c, and HZL1−3 were intravenously injected into KM mice (n = 3). The mice were then placed in the supine posture, and whole-body NIR-II fluorescence images were obtained at various time points. After that, the animals were euthanized, and the main organs were dissected for *ex vivo* biodistribution imaging. ImageJ software was used to assess the fluorescence intensity of the bladder, liver and leg *in vivo* images and the intestine and liver in *ex vivo* biodistribution images to calculate the ratios of liver to leg, bladder to leg and intestine to liver.

For the quantification of probes through hepatobiliary and urinary excretion in 24-h urine and feces, urines or feces were collected from female KM mice 24 h after injection of CH1055a-c, H3a-c, or HZL1−3 in the metabolic cage. The dye content in feces and urine samples was measured using an NIR-II *in vivo* imaging system. The excretion ratio was calculated using Eq. (2):

$$\text{Excretion ratio}\,(\%) = 100 \times \frac{\text{Dye content in feces or urines}}{\text{Injected dye amount}} \quad (2)$$

2.12. Establishment of the biliary atresia mouse model

Female KM mice were assigned to three groups: sham operation, bile duct stricture (BDS), or bile duct ligation (BDL). All animals were anesthetized by intraperitoneal injection of pentobarbital sodium (50 mg/kg) and underwent laparotomy *via* an upper-midline incision to locate the bile duct near the top edge of the pancreas. The common bile duct was carefully isolated from the lateral portal vein and hepatic artery and ligated twice for the BDS group (6-0 silk suture) or ligated doubly and transected between the ligatures for the BDL group. For the sham group, the common bile duct was only isolated without ligation or transection. Finally, a 4-0 absorbable suture was used to close the abdomen in layers, and the animals were awakened with a heating pad.

2.13. In vivo imaging and pharmacokinetic studies in biliary atresia mice

Mice from the sham, BDS, and BDL groups were randomly assigned for NIR-II fluorescence imaging on the 1st, 7th, and 14th days after surgery (n = 3). HZL2 was intravenously injected into mice in the sham, BDS, and BDL groups (n = 3, i.v., 15 mg/kg, 200 μL). Real-time NIR-II fluorescence imaging was performed at different time points after HZL2 injection. For pharmacokinetic studies in biliary atresia mice, blood samples were obtained at various time points (5, 10, 15, 20, 30, 60, 120, 240, 360, 480, 600, 720, and 1440 min) post-injection of HZL2 and then quantified using NIR-II imaging. Finally, the mice were euthanized after *in vivo* imaging. Major organs were collected for NIR-II biodistribution imaging and fixed in 4% paraformaldehyde for histological examination.

2.14. Biochemical analysis

Blood samples obtained from the mouse orbital were quickly frozen and stored at −80 °C for further biochemical analysis. For the model evaluation of the sham, BDS, and BDL groups, serum aspartate aminotransferase (AST), alanine aminotransferase (ALT), and total bilirubin (TBIL) levels were measured. For *in vivo* safety assessment of HZL2, the levels of AST, ALT, TBIL, total cholesterol (TC), blood urea nitrogen (BUN), and creatinine were measured by serum biochemical analysis.

2.15. Histological analysis

Tissues including the heart, liver, spleen, lung, and kidney were fixed with 4% paraformaldehyde buffer, embedded in paraffin, sectioned, and stained with hematoxylin and eosin for histological analysis.

2.16. Statistical analysis

Student's t test or one-way analysis of variance (ANOVA) was performed when comparing two groups or more than two groups, respectively. Statistical analysis was performed using GraphPad Prism version 8.0. Data were expressed as the means ± SD. Differences were considered to be significant if $P < 0.05$ ($^*P < 0.05$, $^{**}P < 0.01$, $^{***}P < 0.001$, $^{****}P < 0.0001$ unless otherwise indicated).

3. Results and discussion

3.1. Rational design, synthesis and characterization of novel hepatobiliary excreted NIR-II probes

In general, the lipid solubility of probes has a significant impact on the excretion of organic molecules. Small and hydrophilic organic

dyes are excreted preferentially by the kidney, while large and amphipathic organic dyes are preferentially excreted through the liver (Scheme 1B)[39]. To obtain amphiphilic NIR-II fluorescent probes that could be rapidly excreted through the hepatobiliary system, 6 amphiphilic NIR-II probes (CH1055a-c and H3a-c, shown in Fig. 1A and C) were first designed and analyzed[36,37]. CH1055a-c and H3a-c were synthesized in a concise way and fully characterized by matrix-assisted laser desorption/ionization time-of-flight mass spectrometry (MALDI-TOF-MS) (Supporting Information Figs. S1−S6). The effect of different molecular weights of PEG and different skeletons of the donor/space of dyes on the lipid-water partition coefficient (log*P*) were studied using *n*-octanol and water. As shown in Fig. 1B and D, the log*P* value order was H3a (n = 7, −0.41) > CH1055a (n = 8, −0.64) > H3b (n = 12, −1.25) > CH1055b (n = 12, −1.47) > H3c (n = 22, −2.16) > CH1055c (n = 20, −2.27). The log*P* value decreased as the polymerization degree of PEG_n increased for the CH1055n and H3n series. The corresponding log*P* value of H3n with fluorene as a donor was higher than that of CH1055n with -$PhNPh_2$ as the donor at similar molecular weights of PEG, revealing that the log*P* value of NIR-II fluorophores could be tuned by the PEG chain length and the fluorene skeleton of the donor.

To evaluate *in vivo* metabolic characteristics and the excretion pathway, CH1055a-c and H3a-c were then administered into KM mice through tail vein injection. NIR-II images were taken at 1 h post-injection. As shown in Fig. 1E, the liver signals decreased and the bladder signals increased when the polymerization degree of PEG increased. Semiquantitative fluorescent analysis was adopted to examine the fluorescence signal ratios of the liver to leg tissue (L/L) or the bladder to leg tissue (B/L). The maximum L/L ratios of CH1055a-c steadily decreased from ∼6, whereas those for H3a-c declined gradually from ∼10 with H3a having the highest L/L value of ∼10. The maximum B/L ratio of CH1055a-c gradually increased from ∼8 to ∼13, while the maximum B/L ratio of H3a-c increased sharply from ∼4 to ∼30 along with the longer PEG chain (Fig. 1F−K). Subsequently, the 24 h excreted urines or feces through mouse metabolic cages were collected after tail vein injection. NIR-II fluorescence imaging was further used to quantify the percentages of CH1055a-c and H3a-c eliminated by the kidney or liver in 24 h. As demonstrated in Supporting Information Fig. S7, the experimental results of 24 h excretion further validated the conclusions in Fig. 1E−K. The 24 h excretion through the liver order was H3a (∼47%) > CH1055a (∼19%) > CH1055b (∼11%) > H3b (∼3%) > CH1055c (∼0%) ≈ H3c (∼0%). The half-life of H3a in the blood circulation was found to be ∼56 min (Supporting Information Fig. S8). From the half-life data and negligible renal excretion, the liver elimination rate constant of H3a was ∼0.74 h^{-1}. These results revealed that H3a, excreted by the liver, corresponded to a higher log*P* value (−0.41).

However, H3a still does not meet the requirement for biliary atresia diagnosis. Therefore, we further optimized and tuned the substituent groups on the sp^3 carbon of the fluorene group of H3 to increase the lipid solubility and liver excretion ability. The benzyl group has been widely employed to enhance the lipid solubility of medications and improve the pharmacokinetic features of pharmaceuticals, such as phenoxybenzamine and benzylpenicillin[40,41]. Thus, a novel NIR-II fluorophore, HZL, with a benzyl substituted group was designed and synthesized. Then, HZL1−3 with a higher polymerization degree of PEG_n (n = 12−44) were designed and synthesized to match the molecular weight of H3a-c (Fig. 2A). As shown in Fig. 2A, HZL was prepared at ∼20% overall yield *via* an efficient synthetic route from unsymmetrical 9,9-disubstituted fluorene. The PEGylated NIR-II fluorescent probes HZL1−3 were then obtained by the integration of PEG with different chain lengths to improve the water solubility and biocompatibility (Fig. 2A). The structures of all intermediates and final products were analyzed by ^{1}H NMR, ^{13}C NMR and ESI-MS or MALDI-TOF-MS (Supporting Information Fig. S9−S19, S22−S24). Vis-NIR absorption and NIR-II fluorescence emission spectra of HZL and HZL1−3 were investigated (Fig. S20 and Fig. 2B−C). The absorption of HZL1−3 peaked at ∼750−∼800 nm, and the emission peaked at ∼1000−∼1070 nm in aqueous solution. A bathochromic shift was observed in the case of HZL1−3 compared to HZL. Furthermore, high quantum yields of HZL in dichloromethane or HZL1, HZL2, and HZL3 in aqueous solution were determined to be 15.2%, 0.82%, 0.98%, and 0.94%, respectively ($QY_{IR\text{-}26}$ = 0.5% in 1,2-dichloroethane, Supporting Information Figs. S21 and S25).

HZL1−3 is composed of hydrophilic polyethylene glycol chains and hydrophobic aromatic chromophores, which can self-assemble into stable micelles in aqueous solution. The critical aggregation concentrations (CACs) of HZL1, HZL2, and HZL3 were determined to be 0.107, 0.140, and 0.187 mg/mL, respectively (Supporting Information Fig. S26). The longer PEG chains may contribute to a high value of CAC and high water solubility[43]. The aggregates were further characterized by dynamic light scattering (DLS) and transmission electron microscopy (TEM). As illustrated in Fig. 2D−F and Supporting Information Fig. S27, the results showed that HZL1 (220 ± 80 nm), HZL2 (240 ± 30 nm), and HZL3 (150 ± 40 nm) generated spherical particles in aqueous solution, and the particle size decreased as the hydrophilic chain length increased. The water dispersion system of HZL1−3 had high stability due to the large zeta potentials of HZL1 (−24.3 ± 1.9 mV), HZL2 (−22.4 ± 0.5 mV), and HZL3 (−20.3 ± 0.3 mV) (Supporting Information Fig. S28). The theoretical log*P* (XLOGP2, XLOGP3 and miLog*P*) values were calculated to assess the excretion properties using the atom or fragment addition methods (Fig. 2G)[42]. HZL1−3 exhibited higher log*P*, XLOGP2, XLOGP3 and miLog*P* values than H3a-c with similar molecular weights and hydrophobic and hydrophilic groups (Fig. 1D and 2G and H), respectively, indicating high potential hepatobiliary excretion.

To further explore the capability of these probes for *in vivo* imaging, HZL1−3 was injected into mice *via* the tail vein, and the half-life of blood circulation of HZL1−3 was measured by the blood fluorescence intensity at different time points fitted by first-order exponential decay. As shown in Supporting Information Fig. S29, the blood circulation half-life of HZL1−3 increased with increasing molecular weight of PEG by evading reticuloendothelial system clearance ($t_{1/2,\ HZL1}$ = 54 min, $t_{1/2,\ HZL2}$ = 179 min, and $t_{1/2,\ HZL3}$ = 418 min). Bright NIR-II fluorescence signals were identified in the intestine at intervals of 2−6 h after tail vein injection of HZL2 (Fig. 3A). Surprisingly, it was also demonstrated that HZL1−3 could be secreted into bile by hepatocytes in a short period of time and excreted to the intestines *via* the gallbladder and bile duct (Fig. 3B−D). The intestinal tract of mice injected with HZL2 displayed the strongest NIR-II fluorescence signals (Fig. 3C). Subsequently, we performed semi-quantitative analysis of fluorescence signals from the intestine and liver using ImageJ software. As shown in Fig. 3E, the *ex vivo* fluorescent signal ratio of the intestinal tract to the liver (I/L) of HZL2 was ∼5. The proportion of

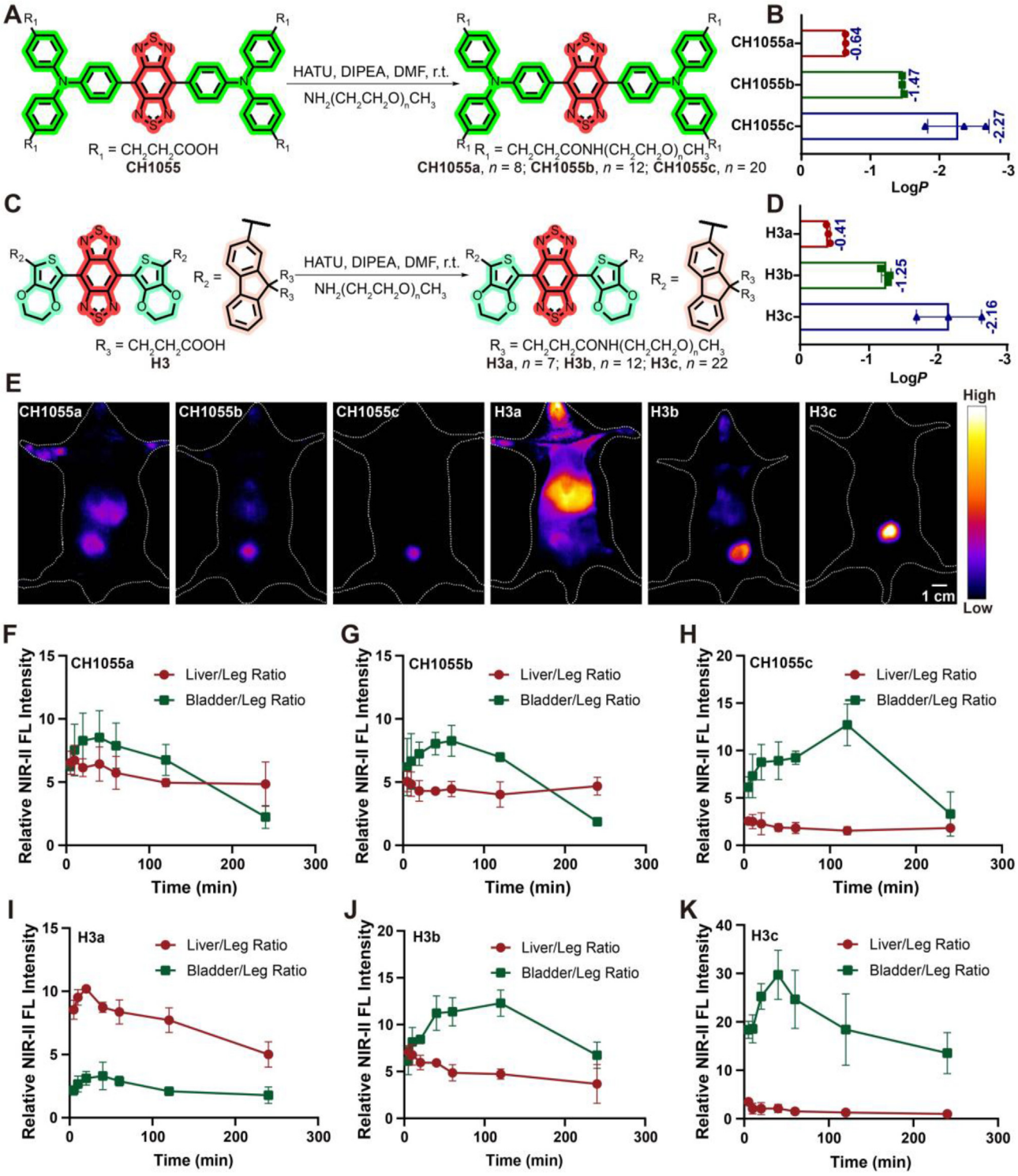

Figure 1 The strategy for tuning the excretion pathway of CH1055a-c and H3a-c. (A−D) The preparation methods, structures, and experimental log*P* values determined in *n*-octanol and water of CH1055a-c and H3a-c ($n = 3$). (E) The representative *in vivo* NIR-II fluorescence images (1000 LP and 200 ms) for the probe excretion of KM mice at 1 h after tail vein injection of CH1055a-c and H3a-c under an 808 nm excitation (90 mW/cm^2), scale bar: 1 cm. (F−K) The change trend of NIR-II fluorescence signal ratio (liver to leg ratio and bladder to leg ratio) at 5, 10, 20, 40, 60, 120, and 240 min after tail vein injection of CH1055a-c and H3a-c ($n = 3$).

HZL1−3 excreted by 24-h feces was quantified using NIR-II fluorescence imaging and is presented in Fig. 3F−G, revealing that HZL2 has a superior hepatobiliary excretion capacity (~80%) and a suitable lipid-water partition coefficient (log*P* = −0.61, Fig. 2H)[44]. All these results suggest that HZL2 has potential for the *in vivo* diagnosis of bile duct-related diseases.

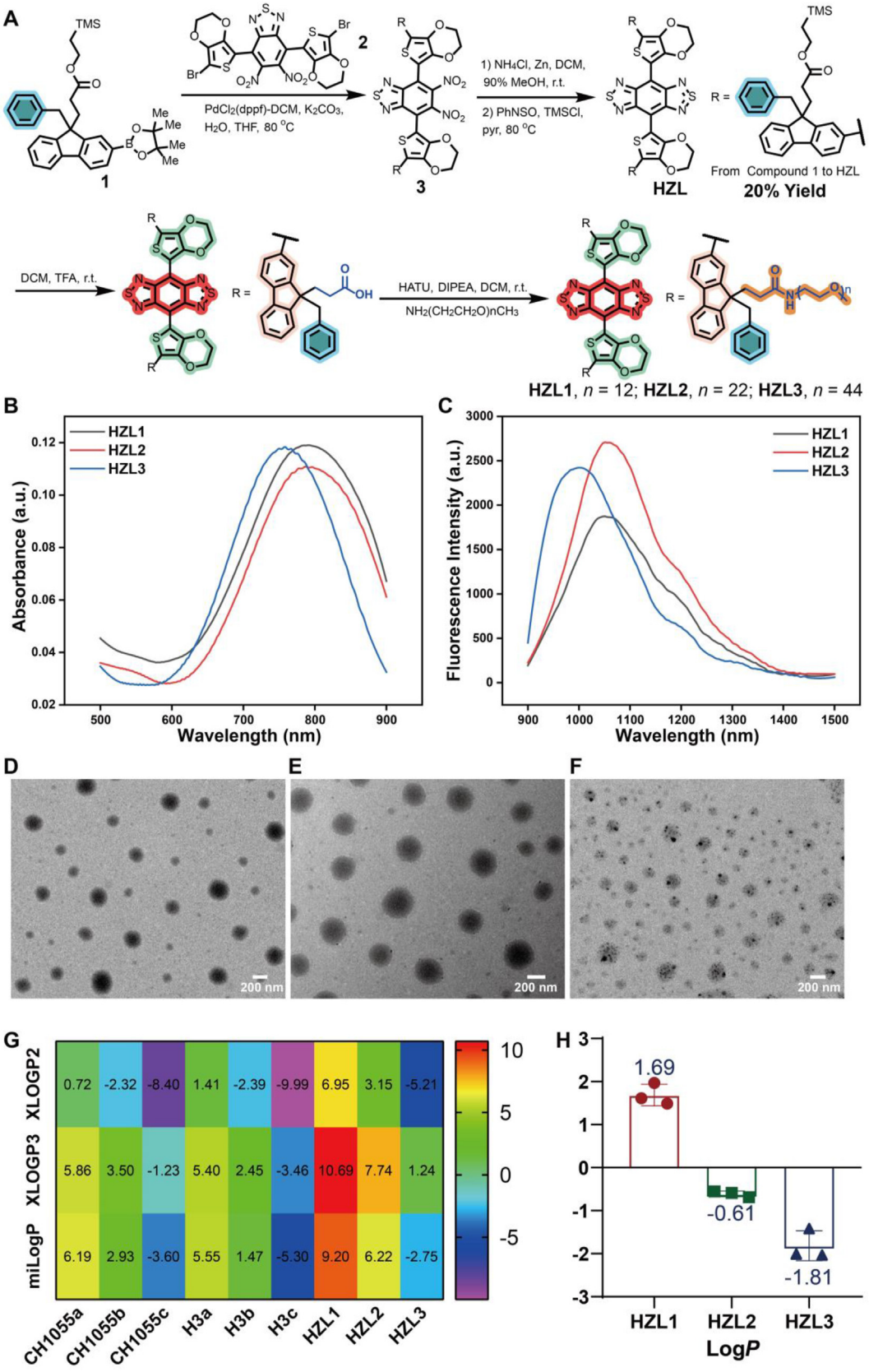

Figure 2 Preparation and characterization of HZL and HZL1−3. (A) Facile preparation route of the small-molecule dye HZL and HZL1−3. (B−C) Vis−NIR absorption spectra (B) and NIR-II fluorescence emission spectra (C) of HZL1−3 in aqueous solution under 808 nm laser excitation. (D−F) TEM images illustrate the self-assembling properties of HZL1 (D), HZL2 (E) and HZL3 (F) in aqueous solution, scale bar: 200 nm. (G) The heatmap of the results from theoretical log*P* calculation (XLOGP2, XLOGP3, and miLog*P*)[42] for CH1055a-c, H3a-c, and HZL1−3. (H) The experimental log*P* values of probe HZL1−3 ($n = 3$).

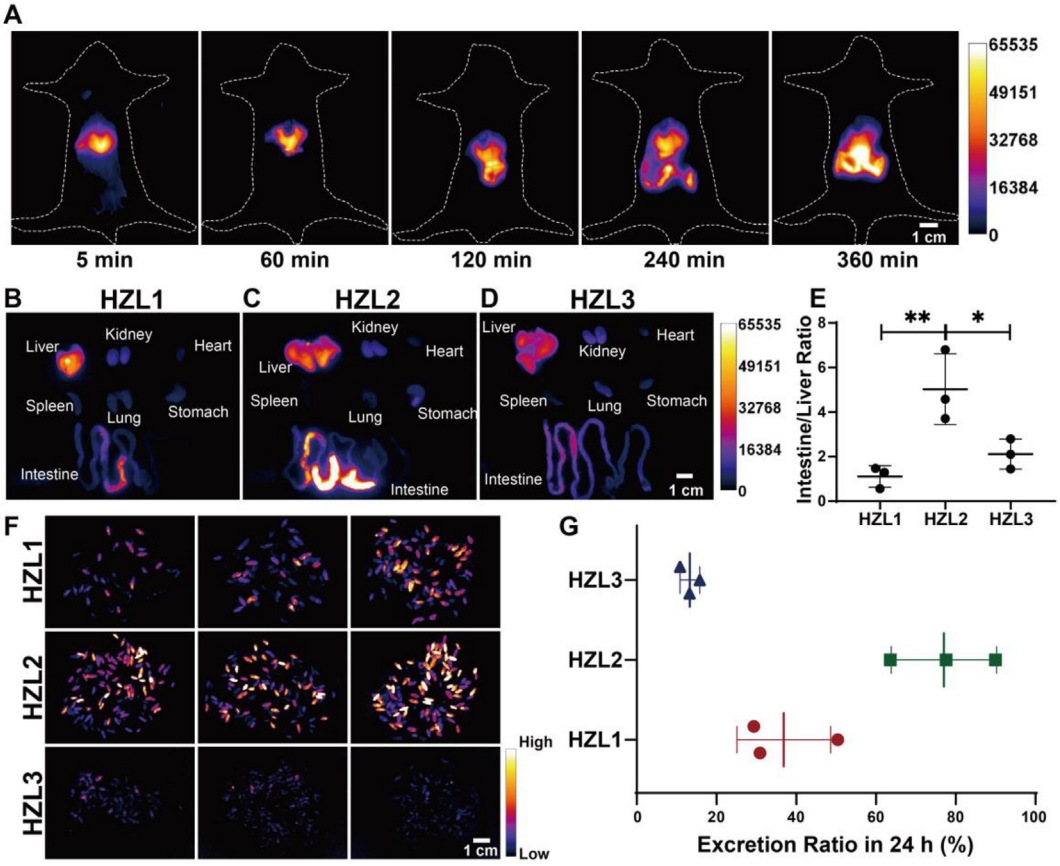

Figure 3 *In vivo* hepatobiliary clearance properties of HZL1−3. (A) The representative *in vivo* NIR-II fluorescence images (1000 LP and 100 ms) of normal KM mice at 5, 60, 120, 240, and 360 min after tail vein injection of HZL2 at a dosage of 15 mg/kg under 808 nm excitation (90 mW/cm^2), scale bar: 1 cm. (B−D) Representative *ex vivo* NIR-II fluorescent imaging (100 ms, 1000 nm LP) of major organs (heart, liver, spleen, lung, kidney, stomach and intestine) dissected from KM mice at 6 h after tail vein injection of HZL1 (B), HZL2 (C), and HZL3 (D) at a dosage of 15 mg/kg, scale bar: 1 cm. (E) The average NIR-II fluorescence intensity ratio of intestine to liver at 6 h after tail vein injection of HZL1−3 (The data are expressed as mean values ± SD, derived from three independent mice). The statistical significance was determined by ordinary one-way ANOVA (*$P < 0.05$ and **$P < 0.01$). (F) NIR-II imaging (1000 LP and 200 ms) of feces within 24 h after tail vein injection of HZL1−3 ($n = 3$), scale bar: 1 cm. (G) The excretion ratio (%) of HZL1−3 through feces within 24 h after tail vein injection ($n = 3$).

3.2. *In vitro and in vivo biosafety evaluation of HZL2*

The biosafety of HZL1−3 was assessed using the CCK8 assay to further investigate their potential for biological applications. As demonstrated in Fig. 4A−C, these probes at various concentrations (0, 10, 20, 30, 40, and 50 μmol/L) showed a discernible difference in cell viability, which remained greater than 80% even at the highest concentration of 50 μmol/L. Additionally, we further verified the biocompatibility of these probes by cell microscopic imaging using a calcein-AM/PI staining kit. The cells treated with 10, 30, and 50 μmol/L probes showed no apparent cytotoxicity compared to the control group and DOX treatment group (Fig. 4D). The erythrocyte cytotoxicity of HZL2 was further evaluated by a hemolysis assay. The hemolysis percentage of HZL2 at high concentrations up to 100 μmol/L was <5%, demonstrating that HZL2 is nonhemolytic and hemocompatible (Supporting Information Fig. S30). Then, HZL2 was injected into mice through the tail vein, and the serum was collected for biochemical examination. As shown in Fig. 4E−J and Supporting Information Fig. S31, there was no significant difference in the results between the PBS control and HZL2 (15 and 150 mg/kg) treatment groups for the liver function including ALT, AST, and TBIL, blood lipid level TC or kidney function including BUN and creatinine. *Ex vivo* pathological analysis of major organs showed that there was no obvious organ damage or inflammatory infiltration in the HZL2 group compared with the PBS group (Fig. 4K), suggesting the safety and high potential clinical use of HZL2.

3.3. *The BDS and BDL models of biliary atresia*

To investigate the potential of HZL2 to diagnose and image biliary atresia, the BDS and BDL groups, as well as a sham group (Fig. 5B) were constructed (Fig. 5). BDS mice exhibited extremely obvious pathological changes compared to the control group, including small body sizes, yellow ears and skin, slower gut peristalsis, massive feces accumulation, and significant serum jaundice (Supporting Information Fig. S32). As shown in Supporting Information Fig. S33, the skin and viscera of mice were normal throughout the cycle in the sham group and on the first postoperative day in the BDS group, while the skin and gastrointestinal tract of mice exhibited obvious jaundice in the BDL group from the 1st to 14th days and in the BDS group from the 7th to 14th days after surgery. On the 14th

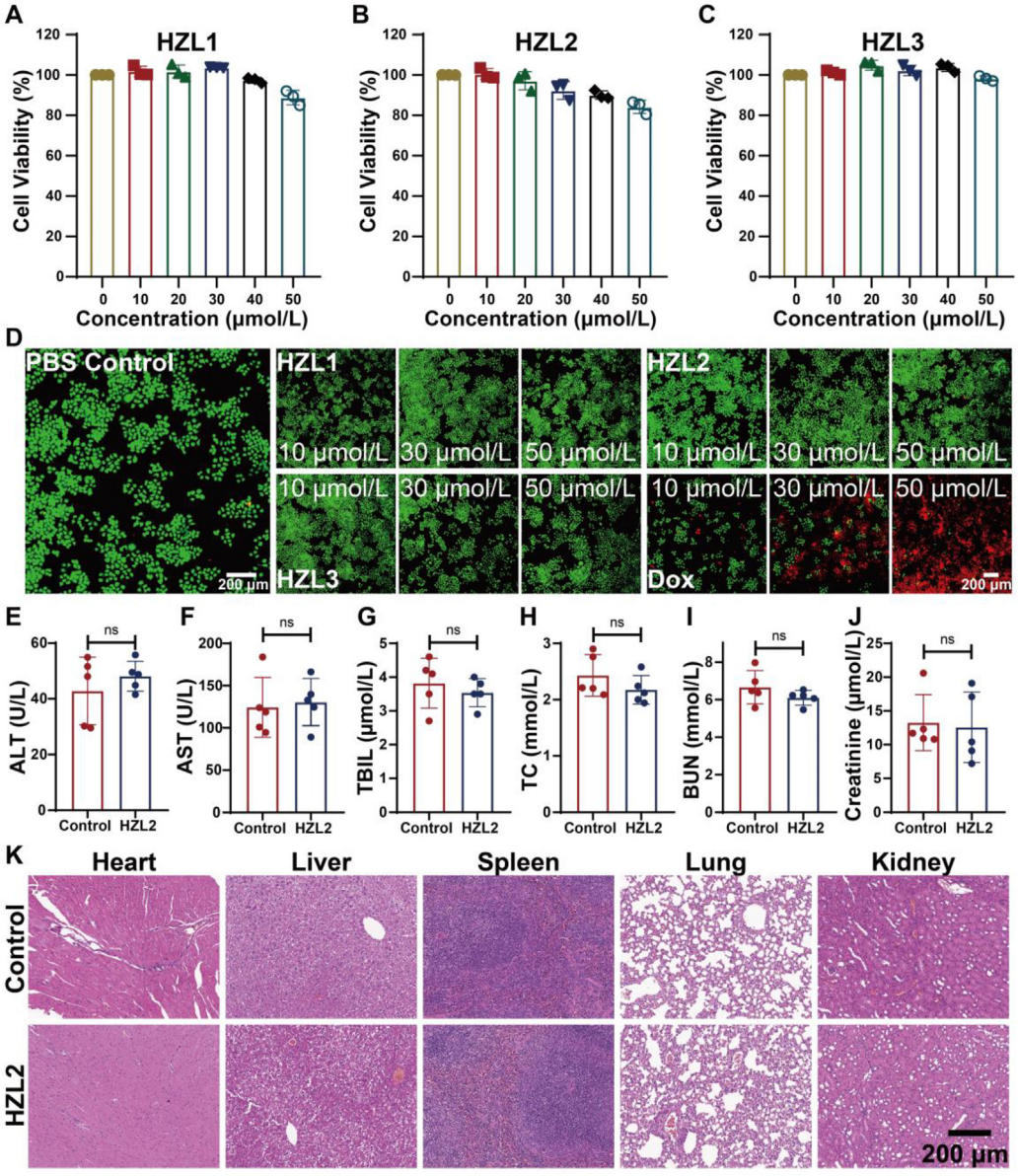

Figure 4 *In vitro* and *in vivo* safety assessment. (A−C) Cell viability of the normal human hepatic cell line L02 cells after incubation with different concentrations (0, 10, 20, 30, 40, 50 μmol/L) of HZL1 (A), HZL2 (B) and HZL3 (C) for 24 h (the data are expressed as mean values ± SD, derived from three independent experiments with five replicates per concentration in each trial). (D) Live/dead cell assessment using fluorescence microscopic imaging stained by calcein-AM/PI of L02 cells after incubation with different concentrations (10, 30, 50 μmol/L) of HZL1−3 and doxorubicin for 24 h. PBS treatment was the negative control group, scale bar: 200 μm. (E−J) The serum biochemistry indexes including ALT (E), AST (F), TBIL (G), TC (H), BUN (I) and creatinine (J) of mice treated with 200 μL PBS or HZL2 solution at a dosage of 15 mg/kg *via* tail vein injection for 15 days (the data are expressed as mean values ± SD, derived from five independent mice). No statistical significance between PBS control and HZL2 treated group was observed, performed by unpaired Student's *t*-test using GraphPad Prism version 8.0. (K) Representative hematoxylin-eosin (H&E) staining of major organs (heart, liver, spleen, lung, and kidney) collected on the 15th day after PBS or HZL2 administration through tail vein injection, scale bar: 200 μm.

day after surgery, the gallbladder and bile duct in the BDS group were enlarged and extremely distended, whereas the liver in the BDL group was severely necrotic (Fig. S33). Serum was obtained on the 1st, 7th, and 14th days after surgery. The hepatic index and levels of ALT, AST, and TBIL in the BDS and BDL groups were significantly greater than those in the sham group (Supporting Information Fig. S34 and Fig. 5E−G). On the 1st, 7th, and 14th days after the operation, the mice were euthanized for histopathological studies with H&E staining (Fig. 5H). Significant inflammatory cell infiltration and hepatocyte necrosis were found in the BDS and BDL groups from the 7th day after the operation (Fig. 5H). These results also indicated that both the BDS and BDL procedures can generate a disease model of cholestasis caused by biliary atresia, with BDL treatment resulting in faster and more severe liver injury (Fig. 5H and Fig. S33).

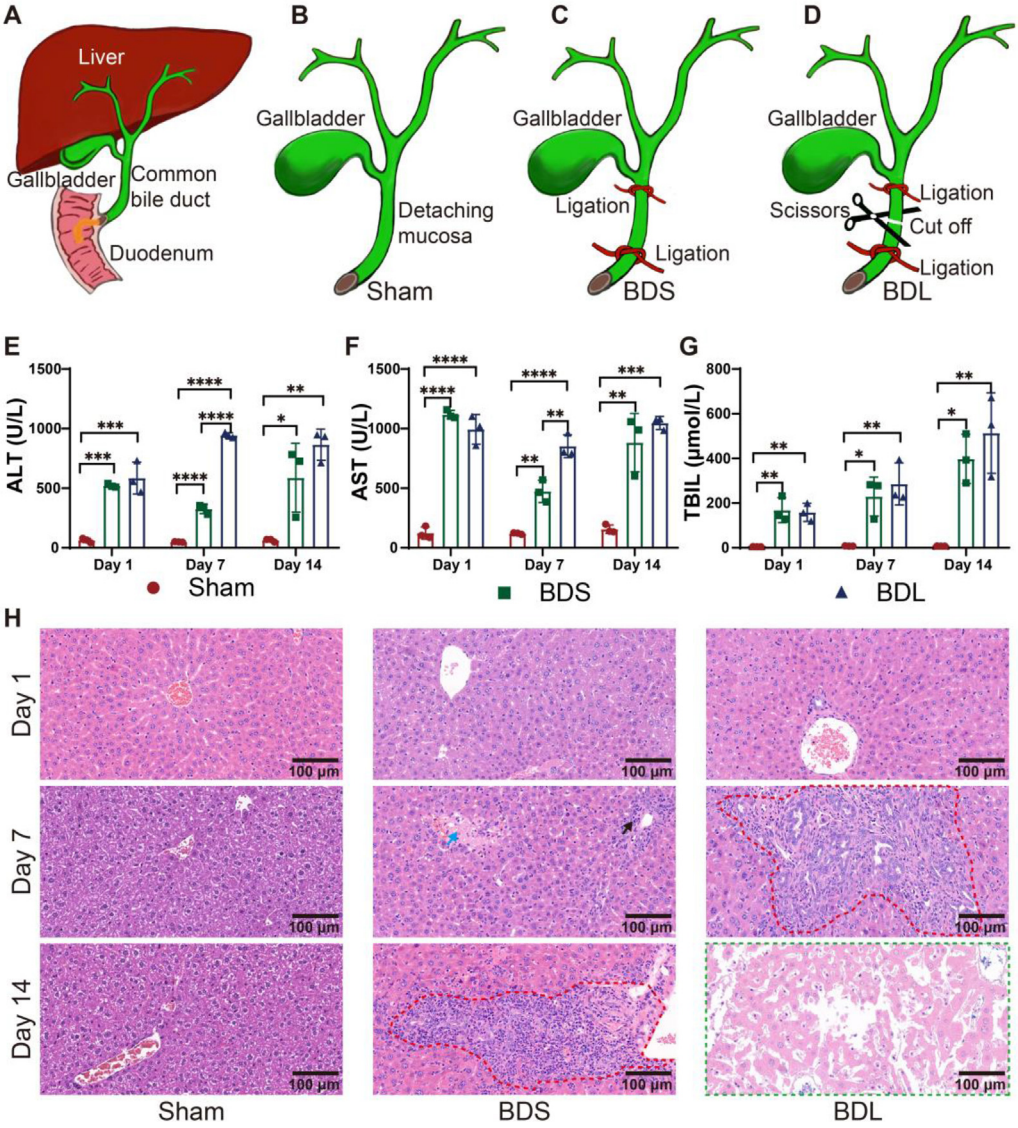

Figure 5 Establishment of mouse biliary atresia model. (A) Schematic depiction for anatomical structure of gallbladder and bile duct that connects with duodenum and liver. (B−D) Schematic diagram of the common bile duct surgery including laparotomy and the common bile duct isolation from the surrounding soft tissues (B, sham), double ligation of the common bile duct (C, BDS), the common bile duct dual ligations and transection between the ligatures (D, BDL). (E−G) Serum alanine aminotransferase (E, ALT), aspartate aminotransferase (F, AST) and total bilirubin (G, TBIL) levels of sham, BDS, and BDL mice on the 1st, 7th, and 14th days after the surgery. The data are expressed as mean values ± SD, derived from three independent mice. The statistical significance was determined by ordinary one-way ANOVA, $^{*}P < 0.05$, $^{**}P < 0.01$, $^{***}P < 0.001$, and $^{****}P < 0.0001$. (H) Representative hematoxylin−eosin (H&E) sections from sham liver (left), BDS liver (middle) and BDL liver (right) on the 1st, 7th, and 14th days after the surgery. Black and blue arrows indicate inflammatory cell infiltration and hepatocyte necrosis, respectively. The coexistence of inflammatory cell infiltration and necrosis is shown in the red dotted area, and all cells in the green dashed box are necrotic. Scale bar: 100 μm.

3.4. In vivo NIR-II fluorescence imaging of biliary atresia using HZL2

Subsequently, the murine BDS and BDL models of biliary atresia were successfully verified by *in vivo* NIR-II fluorescence imaging at 6 h after tail vein injection of HZL2 under 808 nm excitation (90 mW/cm^2). As shown in Fig. 6A, obvious NIR-II fluorescence signals in the gut of KM mice ($n = 3$) were observed in the sham group on the 1st, 7th, and 14th days post-injection of HZL2 (0.2 mL, 15 mg/kg). Fortunately, few signals were detected in the bowel on the 1st day after the operation in the BDS group. There was no fluorescence signal in the gut on the 7th and 14th days in the BDS group or the 1st to 14th days in the BDL group, demonstrating that HZL2 can achieve the early detection of biliary atresia and could be a powerful tool for the development of pathogenesis and therapeutic drugs for biliary atresia.

To further evaluate the ability of HZL2 to identify biliary atresia at the early stage, HZL2 was injected through the tail vein into the BDS and BDL mouse models and the sham group (3 mice per group). The blood of mice was collected at different time points (5−1440 min). As shown in Fig. 6B−D, NIR-II fluorescence signals in the blood of the BDS and BDL groups were

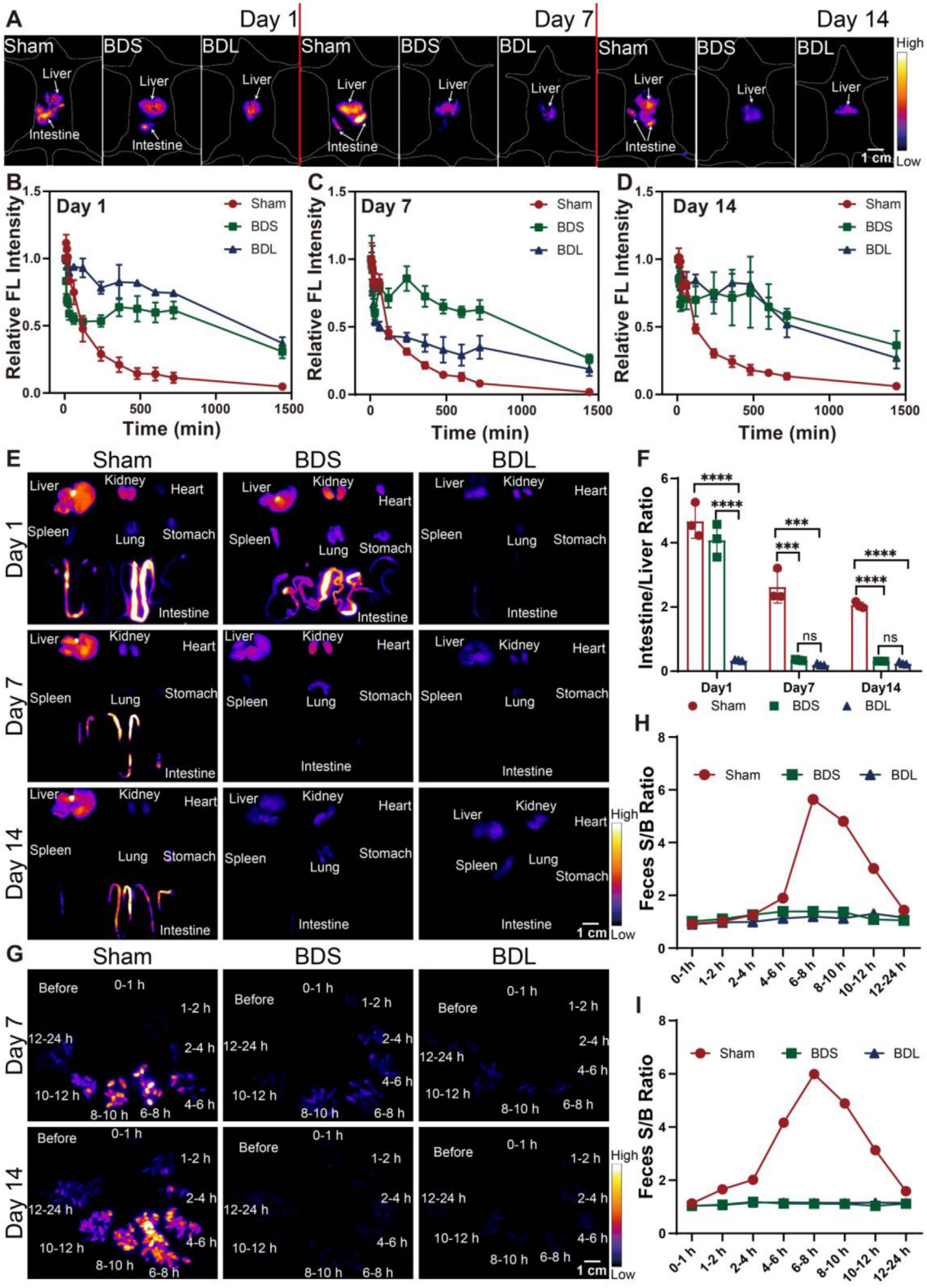

Figure 6 NIR-II fluorescence imaging for biliary atresia using HZL2. (A) The representative *in vivo* NIR-II fluorescence imaging (1000 LP and 50 ms) at 6 h after tail vein injection of HZL2 under an 808 nm excitation (90 mW/cm^2) for sham, BDS, and BDL mice on the 1st (left), 7th (middle), and 14th (right) days after the surgery, scale bar: 1 cm. (B−D) The changes of HZL2 concentration in blood of sham, BDS, and BDL mice on the 1st (B), 7th (C), and 14th (D) days after surgical operation. (E) Representative *ex vivo* NIR-II fluorescent images (50 ms, 1000 nm LP) of major organs (heart, liver, spleen, lung, kidney, stomach, and intestine) which were dissected at 6 h after tail vein injection of HZL2 at a dose of 15 mg/kg from sham, BDS, and BDL mice on the 1st, 7th, and 14th days after surgery, scale bar: 1 cm. (F) The values of intestine-to-liver ratio calculated by fluorescence intensity in *ex vivo* NIR-II images of major organs from sham, BDS, and BDL mice on the 1st, 7th, and 14th days after

obviously stronger than those of the sham group on the 1st, 7th, and 14th days after surgery. Furthermore, *ex vivo* biodistribution of major organs revealed that there were no apparent NIR-II fluorescence signals in the gallbladder and intestine on the 7th and 14th days in the BDS and BDL groups (intestine-to-liver ratio = ~0.5) as well as the first day in the BDL group (intestine-to-liver ratio = ~0.5), suggesting that HZL2 was predominantly deposited in the blood and could not be taken up and expelled by the liver (Fig. 6E−F). Finally, the feces were collected for NIR-II analysis. The feces in the sham group on the 7th and 14th days after surgery had intensive NIR-II fluorescence signals (feces S/B_{max} = ~6), whereas the BDS and BDL groups had no significant NIR-II fluorescence signals in the feces (feces S/B_{max} = ~1) using HZL2 (Fig. 6G−I). Furthermore, the results shown in Supporting Information Fig. S35 demonstrate that HZL2 administration does not amplify the extent of hepatic or renal injury in BDL mice, suggesting that the accumulation of HZL2 is not a significant safety concern for biliary atresia patients. These findings indicate that HZL2 could be adopted to analyze a simple fecal sample for the early detection of biliary atresia.

4. Conclusions

Biliary atresia is the most common cause of liver transplantation in children worldwide. While early detection of biliary atresia is crucial for diagnosis and disease progression, early diagnosis of biliary atresia remains challenging. In this study, we have successfully developed a small-molecule NIR-II fluorescent probe through rational design for *in vivo* NIR-II imaging of biliary atresia with deep penetration depth and high resolution, as well as noninvasive early diagnosis of the disease with exceptional convenience, accuracy and reliability. The water-soluble and biocompatible probe HZL2 which can form spherical nanoparticles by self-assembly in aqueous solution has been synthesized and extensively characterized. It exhibited high photoluminescence intensity and rapid hepatobiliary excretion. The ultrahigh hepatobiliary clearance efficacy of HZL2 coupled with a simple fecal sample allows for the successful and ultrasensitive detection of biliary atresia in the mouse model and early diagnosis of the disease by a noninvasive method. *In vitro* and *in vivo* results suggest that our findings not only open up new avenues for translating the NIR-II probe for *in vivo* early diagnosis of biliary atresia but also provide a research tool for the discovery of pathogenesis and therapeutic drugs for biliary atresia.

Acknowledgments

This work was partially supported by grants from the National Key R&D Program of China (2020YFA0908800), NSFC (82273796), Special Funds for Guiding Local Science and Technology Development of Central Government (XZ202202YD0021C, China), Tibet Autonomous Region COVID-19 Prevention and Control Programs for Science and Technology Development (XZ202201ZY0046G, China), Guangdong Basic and Applied Basic Research Foundation (2023A1515012649, China), Shenzhen Science and Technology Research Grant (JCYJ20220530140605012, China), Translational Medicine and Interdisciplinary Research Joint Fund of Zhongnan Hospital of Wuhan University (ZNJC202209, China), Project Funded by China Postdoctoral Science Foundation (2022M712091, China), the Fundamental Research Funds for the Central Universities. We also thank Xiuli Zhang for her assistance to this effort of schematic drawing.

Author contributions

Xiaodong Zeng: conceptualization, methodology, visualization, writing-original draft, writing-review & editing, project administration. Yuqin Liao: methodology, investigation, validation, visualization, formal analysis, writing-original draft. Xue Qiao: investigation, validation. Ke Liang: investigation, validation. Qiusi Luo: investigation, validation. Mingbo Deng: investigation, validation. Yishen Liu: investigation, validation. Weijing Zhang: investigation, validation. Xuechuan Hong: conceptualization, writing-review & editing, supervision, funding acquisition. Yuling Xiao: conceptualization, writing-review & editing, funding acquisition.

Conflicts of interest

The authors declare no conflicts of interest.

Appendix A. Supporting information

Supporting data to this article can be found online at https://doi.org/10.1016/j.apsb.2023.07.005.

References

1. Hartley JL, Davenport M, Kelly DA. Biliary atresia. *Lancet* 2009;**374**:1704−13.
2. Verkade HJ, Bezerra JA, Davenport M, Schreiber RA, Mieli-Vergani G, Hulscher JB, et al. Biliary atresia and other cholestatic childhood diseases: advances and future challenges. *J Hepatol* 2016;**65**:631−42.
3. Esteves E, Clemente Neto E, Ottaiano Neto M, Devanir Jr J, Esteves Pereira R. Laparoscopic Kasai portoenterostomy for biliary atresia. *Pediatr Surg Int* 2002;**18**:737−40.
4. Hopkins PC, Yazigi N, Nylund CM. Incidence of biliary atresia and timing of hepatoportoenterostomy in the United States. *J Pediatr* 2017;**187**:253−7.
5. Wang J, Xu Y, Chen Z, Liang J, Lin Z, Liang H, et al. Liver immune profiling reveals pathogenesis and therapeutics for biliary atresia. *Cell* 2020;**183**:1867−83.
6. Girard M, Panasyuk G. Genetics in biliary atresia. *Curr Opin Gastroenterol* 2019;**35**:73−81.
7. Asai A, Miethke A, Bezerra JA. Pathogenesis of biliary atresia: defining biology to understand clinical phenotypes. *Nat Rev Gastroenterol Hepatol* 2015;**12**:342−52.

surgery after 6 h by tail vein injection of HZL2 at a dose of 15 mg/kg. The data are expressed as mean values ± SD, derived from three independent mice. The statistical significance was determined by ordinary one-way ANOVA, ***$P < 0.001$ and ****$P < 0.0001$, ns indicates no statistical significance. (G) The representative NIR-II fluorescent images (100 ms, 1000 nm LP) of feces (3 mice per group) collected at different time periods (0−1, 1−2, 2−4, 4−6, 6−8, 8−10, 10−12, 12−24 h) before or after tail vein injection of HZL2 into sham, BDS, and BDL mice on the 7th and 14th days after surgery, scale bar: 1 cm. (H−I) Semiquantitative analysis of feces S/B ratio value (NIR-II fluorescence signals of feces after HZL2 injection/the signals before injection) in Fig. 6G on the 7th (H) and 14th (I) days after the model establishment surgery.

8. Schreiber RA, Harpavat S, Hulscher JBF, Wildhaber BE. Biliary atresia in 2021: epidemiology, screening and public policy. *J Clin Med* 2022;**11**:999.
9. Gilmour SM, Hershkop M, Reifen R, Gilday D, Roberts EA. Outcome of hepatobiliary scanning in neonatal hepatitis syndrome. *J Nucl Med* 1997;**38**:1279−82.
10. Kim H, Park S, Ha S, Kim JS, Kim DY, Oh M. False-negative hepatobiliary scintigraphy for biliary atresia. *Nucl Med Mol Imaging* 2019;**53**:356−60.
11. Abalo KD, Rage E, Leuraud K, Richardson DB, Le Pointe HD, Laurier D, et al. Early life ionizing radiation exposure and cancer risks: systematic review and meta-analysis. *Pediatr Radiol* 2021;**51**:45−56.
12. Yang P, Zhou X, Zhang J, Zhong J, Zhu F, Liu X, et al. Natural polyphenol fluorescent polymer dots. *Green Chem* 2021;**23**:1834−9.
13. Yang P, Zhang S, Chen X, Liu X, Wang Z, Li Y. Recent developments in polydopamine fluorescent nanomaterials. *Mater Horiz* 2020;**7**:746−61.
14. Liu Y, Zhen Y, Tian T, Wang W, Nong J, Qiao X, et al. Novel CD-MOF NIR-II fluorophores for gastric ulcer imaging. *Chin Chem Lett* 2021;**32**: 3061−5.
15. Li J, Liu Y, Xu Y, Li L, Sun Y, Huang W. Recent advances in the development of NIR-II organic emitters for biomedicine. *Coord Chem Rev* 2020;**415**:213318.
16. Li Y, Liu Y, Li Q, Zeng X, Tian T, Zhou W, et al. Novel NIR-II organic fluorophores for bioimaging beyond 1550 nm. *Chem Sci* 2020;**11**: 2621−6.
17. Zhou H, Zeng X, Li A, Zhou W, Tang L, Hu W, et al. Upconversion NIR-II fluorophores for mitochondria-targeted cancer imaging and photothermal therapy. *Nat Commun* 2020;**11**:6183.
18. Chen H, Shou K, Chen S, Qu C, Wang Z, Jiang L, et al. Smart self-assembly amphiphilic cyclopeptide-dye for near-infrared window-II imaging. *Adv Mater* 2021;**33**:2006902.
19. Liu Y, Li Q, Gu M, Lu D, Xiong X, Zhang Z, et al. A second near-infrared Ru (II) polypyridyl complex for synergistic chemo-photothermal therapy. *J Med Chem* 2022;**65**:2225−37.
20. Zheng Y, Li Q, Wu J, Luo Z, Zhou W, Li A, et al. All-in-one mitochondria-targeted NIR-II fluorophores for cancer therapy and imaging. *Chem Sci* 2020;**12**:1843−50.
21. Wu D, Liu S, Zhou J, Chen R, Wang Y, Feng Z, et al. Organic dots with large π-conjugated planar for cholangiography beyond 1500 nm in rabbits: a non-radioactive strategy. *ACS Nano* 2021;**15**:5011−22.
22. Liu Y, Li Y, Koo S, Sun Y, Liu Y, Liu X, et al. Versatile types of inorganic/organic NIR-IIa/IIb fluorophores: from strategic design toward molecular imaging and theranostics. *Chem Rev* 2022;**122**:209−68.
23. Li Y, Gao J, Wang S, Li S, Hou X, Pan Y, et al. Organic NIR-II dyes with ultralong circulation persistence for image-guided delivery and therapy. *J Controlled Release* 2022;**342**:157−69.
24. Liu Y, Gu M, Ding Q, Zhang Z, Gong W, Yuan Y, et al. Highly twisted conformation thiopyrylium photosensitizers for *in vivo* near infrared-ii imaging and rapid inactivation of coronavirus. *Angew Chem Int Ed* 2023;**62**:e202214875.
25. Cheng X, Zhang C, Shen K, Liu H, Bai C, Ding Q, et al. Novel diketopyrrolopyrrole NIR-II fluorophores and DDR inhibitors for *in vivo* chemo-photodynamic therapy of osteosarcoma. *Chem Eng J* 2022;**446**:136929.
26. Li Q, Liu Y, Zhao B, Lei J, Lu S, Gong W, et al. A single-molecular ruthenium (II) complex-based NIR-II fluorophore for enhanced chemo-photothermal therapy. *Chem Commun* 2022;**58**:6546−9.
27. Hu Z, Fang C, Li B, Zhang Z, Cao C, Cai M, et al. First-in-human liver-tumour surgery guided by multispectral fluorescence imaging in the visible and near-infrared-I/II windows. *Nat Biomed Eng* 2020;**4**:259−71.
28. Li Y, Gao J, Wang S, Du M, Hou X, Tian T, et al. Self-assembled NIR-II fluorophores with ultralong blood circulation for cancer imaging and image-guided Surgery. *J Med Chem* 2022;**65**:2078−90.
29. Li Y, Zhu H, Wang X, Cui Y, Gu L, Hou X, et al. Small-molecule fluorophores for NIR-IIb imaging and image-guided therapy of vascular diseases. *CCS Chem* 2022;**4**:3735−50.
30. Sun P, Jiang X, Sun B, Wang H, Li J, Fan Q, et al. Electron-acceptor density adjustments for preparation conjugated polymers with NIR-II absorption and brighter NIR-II fluorescence and 1064 nm active photothermal/gas therapy. *Biomaterials* 2022;**280**:121319.
31. Liu H, Hong G, Luo Z, Chen J, Chang J, Gong M, et al. Atomic-precision gold clusters for NIR-II imaging. *Adv Mater* 2019;**31**: 1901015.
32. Tang L, Zeng X, Zhou H, Gui C, Luo Q, Zhou W, et al. Theranostic gold nanoclusters for NIR-II imaging and photodynamic therapy. *Chem Res Chin Univ* 2021;**37**:934−42.
33. Liang C, Diao S, Wang C, Gong H, Liu T, Hong G, et al. Tumor metastasis inhibition by imaging-guided photothermal therapy with single-walled carbon nanotubes. *Adv Mater* 2014;**26**:5646−52.
34. Yang H, Li R, Zhang Y, Yu M, Wang Z, Liu X, et al. Colloidal alloyed quantum dots with enhanced photoluminescence quantum yield in the NIR-II window. *J Am Chem Soc* 2021;**143**:2601−7.
35. Ding S, Lu L, Fan Y, Zhang F. Recent progress in NIR-II emitting lanthanide-based nanoparticles and their biological applications. *J Rare Earths* 2020;**38**:451−63.
36. Antaris AL, Chen H, Cheng K, Sun Y, Hong G, Qu C, et al. A small-molecule dye for NIR-II imaging. *Nat Mater* 2016;**15**:235−42.
37. Zeng X, Xue L, Chen D, Li S, Nong J, Wang B, et al. A bright NIR-II fluorescent probe for breast carcinoma imaging and image-guided surgery. *Chem Commun* 2019;**55**:14287−90.
38. Zeng X, Xiao Y, Lin J, Li S, Zhou H, Nong J, et al. Near-infrared II dye-protein complex for biomedical imaging and imaging-guided photothermal therapy. *Adv Healthcare Mater* 2018;**18**:1800589.
39. Hagenbuch B. Drug uptake systems in liver and kidney: a historic perspective. *Clin Pharmacol Ther* 2010;**87**:39−47.
40. Zhang Z, Tang W. Drug metabolism in drug discovery and development. *Acta Pharm Sin B* 2018;**8**:721−32.
41. Taft DR. Drug excretion. In: Hacker M, Messer W, Bachmann K, ediors, editors. *Pharmacology*. Academic Press; 2009. p. 175−99.
42. Mannhold R, Poda GI, Ostermann C, Tetko IV. Calculation of molecular lipophilicity: state-of-the-art and comparison of log *P* methods on more than 96,000 compounds. *J Pharm Sci* 2009;**98**:861−93.
43. Han P, Li S, Cao W, Li Y, Sun Z, Wang Z. Red light responsive diselenide-containing block copolymer micelles. *J Mater Chem B* 2013;**1**:740−3.
44. Luciano MP, Namgoong JM, Nani RR, Nam SH, Lee C, Shin IH, et al. A biliary tract-specific near-infrared fluorescent dye for image-guided hepatobiliary surgery. *Mol Pharm* 2019;**16**:3253−60.